physica status solidi a
www.pss-a.com

Fabrication of Nitrogen Vacancy Center-Doped Free-Standing Diamond Photonic Devices via Faraday Cage-Angled Etching

Christian Giese, Patricia Quellmalz, Peter Knittel, Tingpeng Luo, Niklas Mathes, Jan Jeske, Philipp Reinke, and Quankui Yang*

Herein, methods for the fabrication of monolithic diamond integrated photonic devices via Faraday cage-angled etching of functional epitaxial diamond layers are presented. Optimal waveguide width is determined via simulation and the fabrication of nitrogen vacancy (NV) center-doped microring resonators is demonstrated. The performance of the devices is verified via microphotoluminescence as well as cathodoluminescence scans of the in-grown NV centers, revealing clearly visible cavity lines. The scalable fabrication method allows for the realization of large numbers of lateral waveguide structures as needed for future applications in integrated quantum sensing devices as well as novel spin-based quantum computers.

1. Introduction

The negatively charged nitrogen vacancy (NV) center is a localized atomic size defect in the diamond crystal lattice which exhibits extraordinary features, most prominently long spin coherence time at room temperature.[1–5]

Diamond-based photonic integrated circuits (PIC) comprise a platform harnessing its outstanding material properties for the generation, manipulation, and detection of quantum states of light.[6–9] Combining carbon-based photonics and color centers enables miniaturization and scaling of numerous applications, spanning from quantum sensing to quantum information and computing.[10–13]

A limitation of the use of NV centers is the relatively small fraction (around 3%) of emission to the zero-phonon line (ZPL) at 637 nm, as compared to the large-phonon sideband spanning more than a hundred nanometers to the infrared. Purcell enhancement of the ZPL emission by use of cavities is one approach to improve on this issue for single NVs.[12] Due to the high refractive index of diamond (2.4), microring resonators with little bending losses can be realized.[12,13] These devices are important building blocks in integrated photonics commonly used in optical modulators, optical switches, optical frequency combs, sensors or lasers.[14]

Several demonstrations of microring cavities have been based on a diamond-on-insulator platform (DOI).[12,13] In our work, cavities are fabricated via Faraday cage-angled etching of highly nitrogen-doped diamond layers.[14–17] This approach presents several advantages, the most prominent being simplicity of the process chain and efficient use of the bulk diamond material. DOI processes typically require membranes of some 10 μm thickness with surface roughness below 1 nm rms which are expensive and not readily available in high numbers. Furthermore, dry chemical thinning of the diamond layer to below 1 μm is limited to small areas by the membrane wedge. A second approach pioneered by the Prawer group takes advantage of the creation of a graphitized buried layer via MeV energy ion implantation.[18] This method is scalable to larger surfaces and enables for precise control of the diamond membranes. However, the crystal quality of the implanted layers is limited and typically requires a chemical vapor deposition (CVD) overgrowth process. The presented bulk process requires only low-cost diamond substrates and the processable rms surface roughness can be up to two orders of magnitude higher as will be described in detail in the upcoming sections.

2. Experimental Section

High-pressure high-temperature (HPHT) Ib diamond seed crystals were used for the process development and fabrication of the photonic devices. Nitrogen-doped epitaxial overgrowth was performed with subsequent definition of a metal etch mask via electron beam lithography. Finally, the waveguide structures were undercut via inductively coupled plasma (ICP) etching using a Faraday cage.

C. Giese, P. Quellmalz, P. Knittel, T. Luo, N. Mathes, J. Jeske, P. Reinke, Q. Yang
Fraunhofer Institute for Applied Solid State Physics (IAF)
Tullastrasse 72, D-79108 Freiburg, Germany
E-mail: christian.giese@iaf.fraunhofer.de

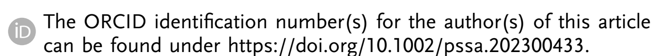
The ORCID identification number(s) for the author(s) of this article can be found under https://doi.org/10.1002/pssa.202300433.

© 2023 The Authors. physica status solidi (a) applications and materials science published by Wiley-VCH GmbH. This is an open access article under the terms of the Creative Commons Attribution License, which permits use, distribution and reproduction in any medium, provided the original work is properly cited.

DOI: 10.1002/pssa.202300433

 © 2023 The Authors. physica status solidi (a) applications and materials science published by Wiley-VCH GmbH

18626319, 2024, 8, Downloaded from https://onlinelibrary.wiley.com/doi/10.1002/pssa.202300433, Wiley Online Library on [24/04/2024]. See the Terms and Conditions (https://onlinelibrary.wiley.com/terms-and-conditions) on Wiley Online Library for rules of use; OA articles are governed by the applicable Creative Commons License

2.1. Diamond Substrates

Microwave plasma-enhanced chemical vapor deposition (MWPECVD) of diamond was carried out for the deposition of intrinsic and thin, nitrogen-doped, functional diamond layers. Details of the growth development have been reported elsewhere.[19,20] For the films used in this work, we employed a 915 MHz reactor with purified gases (hydrogen, methane) to enable growth on a circular area with 6″ diameter for high-throughput processes. All films used were grown on double-side polished HPHT-type Ib diamond seed crystals (MB optics) with low-fluorescent background and roughly 300 μm thickness. For process developments, such substrates were also used either as obtained or after intrinsic overgrowth (≈20 μm after polishing). The N-doped functional layers were deposited on a 4–5 μm intrinsic buffer layer with N/C ratios of 5000 ppm (sample 1) and 20 000 ppm (sample 2). Based on the growth rates and doping efficiencies determined for thicker films grown at the same condition, the N-doped layer had an estimated thickness of 500 nm at 4 ppm p1 density (sample 1) and 700 nm at 15 ppm p1 density (sample 2). Root-mean-square roughness of the as-grown surfaces was determined to be around 15 nm.

2.2. Electron Beam Lithography

In order to define structures below 100 nm lateral dimension, electron beam lithography (Jeol 9500FS) processes were carried out at 100 keV acceleration voltage and 900 μC cm^{-2} dose.

Due to the simplicity of the approach and high lateral resolution, single-layer negative tone resists were commonly relied on. However, there were disadvantages in making use of hydrogen silsesquioxane (HSQ) as etch hard mask on small substrates such as diamond. Inhomogeneities in the layer thickness after spin coating were on the order of hundreds of nanometers and limit the homogeneity and reproducibility of the plasma etching results.

Therefore, in this work, a double-layer polymethyl methacrylate (PMMA) resist was chosen for consecutive metal lift-off. It consisted of a 300 nm-thick MMA/MAA copolymer bottom resist and a 100 nm 950 k PMMA top resist (MicroChem Corp.). Development after exposure was performed with a mixture (3:1) of isopropanol and methyl isobutyl ketone (MIBK) for four minutes. We estimated the minimal achievable critical dimension of our process to be around 50 nm as determined via scanning electron microscopy (SEM). A parameter of importance for etching was the selectivity S defined as the relation between the etch rates of the target material and the mask material. Due to their high selectivity, metal hard masks were chosen. While Titanium was shown to yield $S > 100$, sidewall roughness and redeposition were shown to be an issue during dry etching.[17] Therefore, 80 nm Nickel ($S \approx 20$) was electron beam evaporated. This resulted in visibly reduced sidewall roughness which is critical for waveguide fabrication.

Finally, the lift-of process consisted of a 30-minute acetone dip at a temperature of 40 °C and a consecutive high-pressure dimethyl sulfoxide (DMSO) solvent step at 10 bars of pressure.

2.3. Faraday Cage-Angled Oxygen Dry Etching

The Ni metal hard mask was transferred to the diamond substrate via ICP etching. In order to fabricate lateral diamond waveguides from bulk material, free-standing structures were required. The latter was challenging to realize, and two main approaches were proposed: Faraday cage-angled etching[14–16] and quasi-isotropic dry etching.[21] The former method was used in this work and prior investigations.[17] For this method, a metal cage with angled surfaces was placed over the sample and thus the charged particles within the etch plasma were accelerated toward the target under an angle. **Figure 1** left depicts the cage design in use, consisting of a tent-like aluminum body with clamped stainless steel wire gratings at 45° (250 μm wire diameter and 750 μm mesh pitch).

The center image depicts a conical geometry cage milled from solid aluminum. This type of Faraday cage enables etching from a multitude of directions for circularly symmetric structures. The right side shows a cage for quadridirectional etching in the form of a truncated pyramid. The clamped grating allows for varying the parameters of pitch and gap widths without having to manufacture several cages. These parameters have a significant influence on the angular distribution of the etching ions.[16]

The chosen etching parameters (Sentech SI500) are depicted in **Table 1**. Platen powers were chosen slightly lower than in prior

Table 1. ICP parameters for diamond etch recipes.

Parameter [units]	Pressure [Pascal]	Temperature [°C]	Platen power [W]	ICP power [W]	Oxygen flow [sccm]
vertical etch	1.3	20	45	700	30
FCAE etch	0.6	20	25	700	30

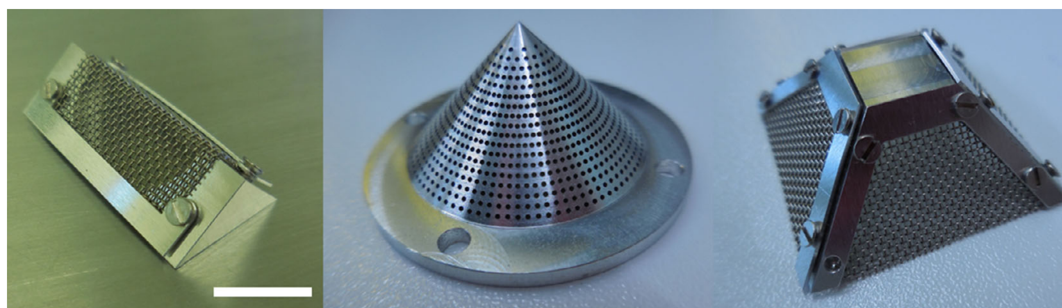

Figure 1. Left: Faraday cage with tent-like geometry for bidirectional etching. Middle: conical-shape Faraday cage for circularly symmetric etching at 45° angle. Right: 60° truncated pyramid geometry cage with clamped wire grating (scalebar 10 mm).

© 2023 The Authors. physica status solidi (a) applications and materials science published by Wiley-VCH GmbH

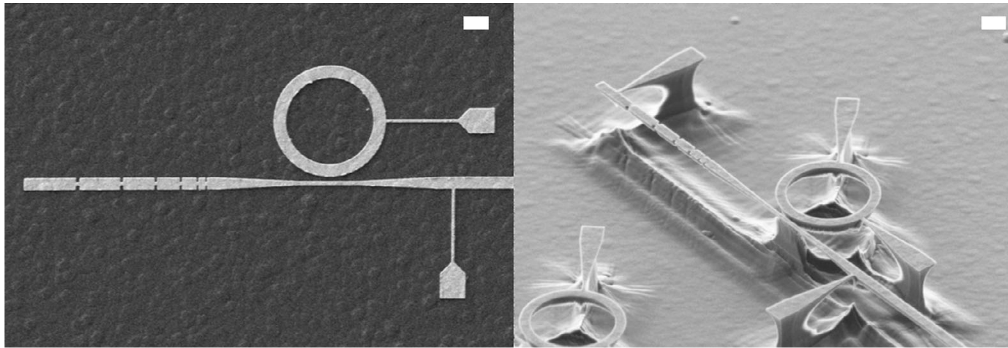

Figure 2. Left: SEM image of 80 nm nickel mask of waveguide structure on sample 1. A microring resonator is placed close to a tapered bus guide terminated by a grating coupler element (1000 nm scalebar). Right: FCAE-etched free-standing device SEM image taken under 30° tilt (1000 nm scalebar).

works in order to protect the hard mask from erosion and redeposition effects. A typical metal mask geometry is shown on the left side of **Figure 2**, featuring critical dimensions below 100 nm.

Prior to the cage process, a 4-minute vertical etch was performed with an increased platen power of 45 W and a pressure of 1.3 Pa. The etch depth was determined to be about 800 nm via laser microscopy (Keyence VK-X200K).

In the next step, the 45° bidirectional cage (Figure 1 left) was placed over the diamond sample. For an approximatively circularly symmetric undercut, the orientation of the cage was switched every 2 min between two alternating positions of 45° and 135° with respect to the (110) sample edge. A typical result is depicted via SEM imaging on the right side of Figure 2 after 28 min total etch time.

Vertical etch rate of the process was verified to be 150 nm per minute while the lateral etch rate was found to be 10 nm/minute with an overall etch depth of 2900 nm. The nickel hard mask edge eroded at a lateral speed of 1.6 nm per min which could be corrected via design bias if required. A variation of the tether geometry was realized for one sample in order to correct for the shrinking due to erosion. While the lateral anchor width was chosen to be 100 nm for the first batch (Figure 2 left), the width was increased to 180 nm (Figure 2 right) and a tapered section was added to the anchor.

In order to visualize the advantages of the monolithic bulk manufacturing, **Figure 3** depicts large-area SEM images of a typical processed diamond sample.

The lift-off process enables structuring of the sample surface up to the edges of the substrate since it suffers less from resist edge beading. 100 fields of $250 \times 250\,\mu m$ size were lithographically defined yielding a total of about 6000 photonic devices per 3×3 mm diamond substrate.

2.4. Optical Simulation

The cross section of the diamond rings and ridges etched by the Faraday cage method is a roughly equilateral triangle, as deduced via SEM. To choose an appropriate lateral width for these triangles, we chose the optical confinement factor of the fundamental mode as the figure of merit. The optical confinement factor Γ can be calculated as

$$\Gamma = \frac{\int_{\text{core}} |E(x,y)|^2 dxdy}{\int_{\text{all}} |E(x,y)|^2 dxdy} \tag{1}$$

where $E(x,y)$ is the electric field distribution, and the x–y plane refers to the cross-section plane. It has been demonstrated in ref. [13] that for a diamond ridge with a square cross section, a width of 300 nm provides sufficient optical confinement to enable meaningful waveguiding. We therefore chose the lateral width of our triangular cross-section ridge to enable the same optical confinement factor as that of a 300 nm square cross-section ridge. The optical confinement factor of the latter is 84%.

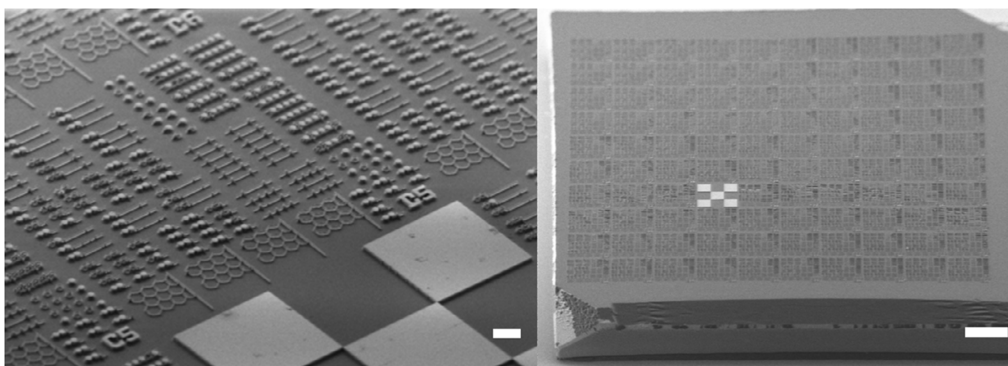

Figure 3. Left: 30° tilted SEM image of typical free-standing lateral waveguide devices. (10 µm scalebar). Right: SEM overview image of diamond sample after processing. (200 µm scalebar).

© 2023 The Authors. physica status solidi (a) applications and materials science published by Wiley-VCH GmbH

18626319, 2024, 8, Downloaded from https://onlinelibrary.wiley.com/doi/10.1002/pssa.202300433, Wiley Online Library on [24/04/2024]. See the Terms and Conditions (https://onlinelibrary.wiley.com/terms-and-conditions) on Wiley Online Library for rules of use; OA articles are governed by the applicable Creative Commons License

physica status solidi a
www.pss-a.com

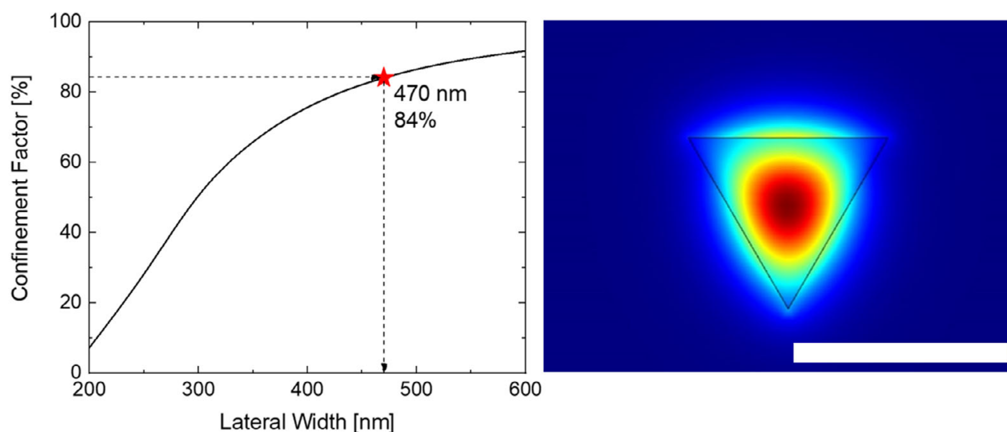

Figure 4. Left: Calculated optical-field confinement factor as a function of the lateral width of the diamond rings and ridges with triangular cross sections. At the width of 470 nm, the optical-field confinement factor reaches a value of 84%, which is equivalent to the value for a ridge with square cross section of 300 nm in width. Right: Calculated cross-sectional electric-field (absolute value, fundamental mode) distribution for a ridge with $w = 470$ nm. The diamond is surrounded by air (500 nm scalebar).

Shown in **Figure 4** (left panel) are the calculated optical-field confinement factors of the fundamental transverse electric mode, as a function of the lateral width of the diamond rings and ridges with triangular cross sections. At the width of 470 nm, the optical-field confinement factor reaches a value of 84%, which is equivalent to the value for a waveguide with square cross section of 300 nm in width and therefore our optimized choice. Figure 4 (right panel) shows the calculated 2D electric field (absolute value |E|) distribution of the fundamental mode for the case $w = 470$ nm. The wavelength used in this calculation was 637 nm corresponding to the NV center ZPL.

A diameter of 4.5 μm was chosen for the microrings in order to directly compare the device to prior work on DOI devices.[8,9]

3. Discussion

The emission properties of the NVs embedded in the processed devices were characterized via wide-field photoluminescence (PL), micro-PL (μ-PL), as well as cathodoluminescence (CL).

3.1. Photoluminescence Characterization

In order to verify the lateral distribution of NV centers, wide-field images were taken in a home-built setup projecting the NV fluorescence onto a camera. An image of sample 1 is depicted on the left side of **Figure 5**. The waist of the excitation beam was roughly 400 μm and excitation power was 300 μW. While the large depth of field of the objective leads to detection of the NV background in the HPHT substrate, the etched devices are visible with high contrast, indicating the complete removal of the NV-doped epitaxial layer around and underneath the structures. This finding is verified via scanning confocal PL scans taken on a home-built setup and displayed for sample 1 on the right side in Figure 5.[22] Excitation wavelength was 532 nm for both measurements.

PL spectra were taken for sample 2 on a number of microrings revealing a set of resonant lines with a maximum of 70% increased detected fluorescence as compared to the incoherent background emission of the NV sidebands. The extracted free spectral range at 680 nm is ≈13 nm (7.9 THz) and agrees well

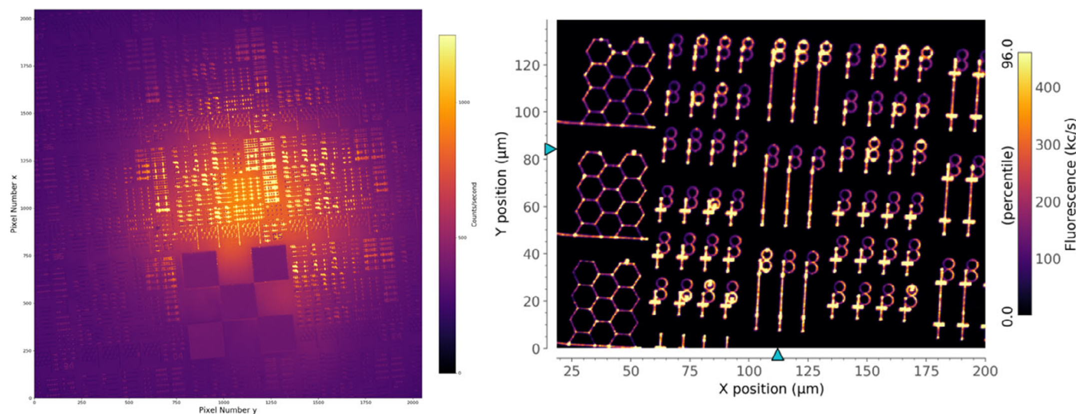

Figure 5. Left: Wide-field PL image of etched diamond sample 1. Right: μ-PL scan of PIC devices of the same substrate. High contrast shows removal of NV-doped layer.

© 2023 The Authors. physica status solidi (a) applications and materials science published by Wiley-VCH GmbH

18626319, 2024, 8, Downloaded from https://onlinelibrary.wiley.com/doi/10.1002/pssa.202300433, Wiley Online Library on [24/04/2024]. See the Terms and Conditions (https://onlinelibrary.wiley.com/terms-and-conditions) on Wiley Online Library for rules of use; OA articles are governed by the applicable Creative Commons License

18626319, 2024, 8, Downloaded from https://onlinelibrary.wiley.com/doi/10.1002/pssa.202300433, Wiley Online Library on [24/04/2024]. See the Terms and Conditions (https://onlinelibrary.wiley.com/terms-and-conditions) on Wiley Online Library for rules of use; OA articles are governed by the applicable Creative Commons License

with the expected value of 13.6 nm. The latter can be calculated in first-order approximation in dispersion and expressed as a wavelength difference with the equation

$$FSR_\lambda = \frac{\lambda^2}{n\,L} \tag{2}$$

With the wavelength λ of 680 nm, the ring circumference L was 14 μm and the diamond's refractive index n was 2.4. Full-width-half-maximum (FWHM) line widths of 1–3 nm were extracted from the data. Finesse (4–9) appears to be low for the investigated type of resonator.

Several factors can hinder the correct measurement of high-quality (Q) factor modes (i.e., the resonant modes of the ring). First, the detected photons in the confocal volume have perpendicular direction of propagation with respect to the ones travelling in the guided modes. Therefore, the measured resonant lines in **Figure 6** originate from leakage or scattering of the guided modes circulating in the lateral plane to the perpendicular detection direction. This means that low-finesse optical modes with high scattering rates could dominate the measurement while high-finesse guided modes are harder to detect since the photons are not emitted vertically from the waveguides. As the waveguides support higher-order lateral modes with enhanced electric field strength close to the sidewalls, this is a possible explanation. Furthermore, narrow lines with low count rates are challenging to identify on the high count-rate background of the isotropic NV sideband fluorescence. Lateral transmission and reflection measurements are necessary to further investigate the matter. Therefore, our setup is currently being modified to allow for displaced excitation. This would enable the independent detection of the guided photons and the isotropically emitted PL signals.

3.2. Cathodoluminescence Characterization

The μ-PL characterizations are limited by optical diffraction to ≈300 nm and therefore CL scans were recorded (Jeol JSM-7610F) to inspect the submicrometer features of the produced cavities. An exemplary scan at 30° tilt angle is depicted in **Figure 7**. On the left-hand side, the SEM image of a device with

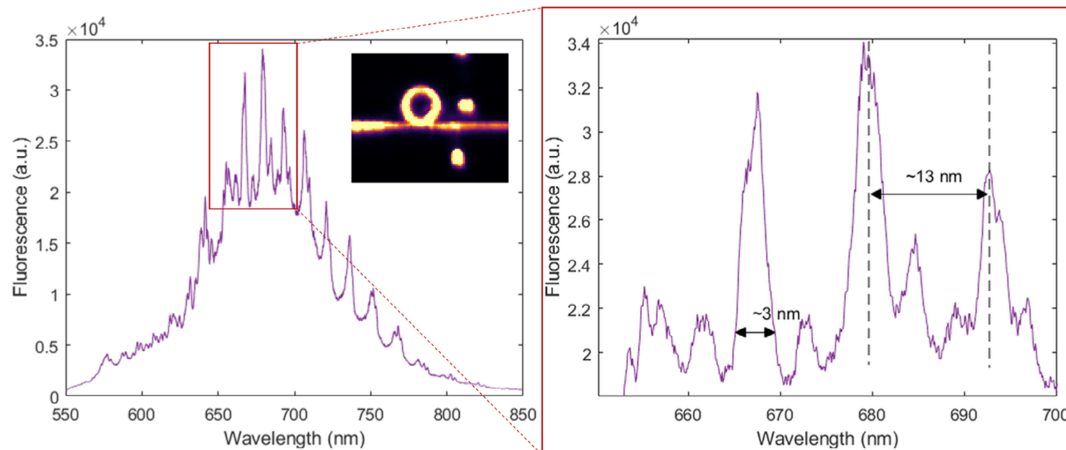

Figure 6. Left: PL spectra of sample 2 as a function of wavelength. Inset: μ-PL scan of the investigated microring. Right: Close-up view of the spectral maximum and the strongest resonant lines.

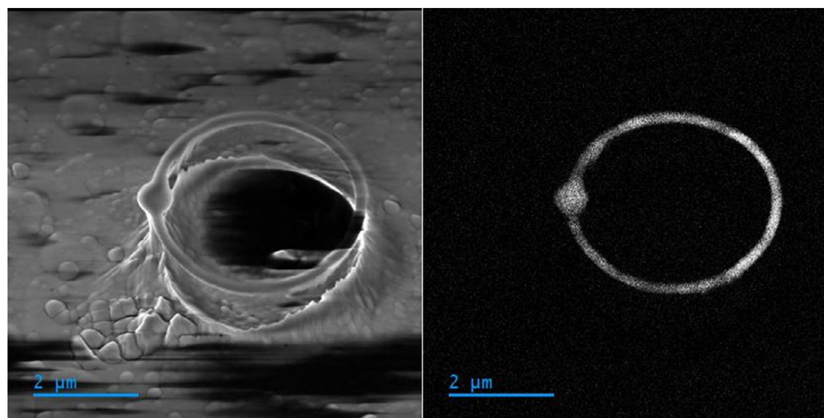

Figure 7. Left: Scanning electron microscope image of a ring resonator with vertical tether on sample 1. Large contrast variation due to charging. Right: CL scan of the structure. The neutral vacancy center is detected with high contrast and in the ring exclusively.

© 2023 The Authors. physica status solidi (a) applications and materials science published by Wiley-VCH GmbH

vertical tether is shown. While charging effects limit the quality of the scan, the essential features are visible. It can be seen that the lateral undercut of the structure is not perfectly circularly symmetric, with one diagonal exhibiting less lateral etching. The sidewall roughness is significantly higher at these points. This is a general issue with cages featuring a low number of etching directions (tent, n-sided pyramid etc.). The side wall roughness is locally increased which we suspect to be the main loss factor decreasing cavity finesse. On the right hand side of Figure 7, the corresponding CL scan is depicted. The method is sensitive only to the neutral charge state of the NV center. NV^0 signal is clearly detected in the ring with very high signal to noise while no color centers are detected in the bulk.

4. Conclusion

In the presented work, we realized scalable, lateral photonic devices via Faraday cage-angled etching from single-crystal bulk diamond with epitaxially grown NV-doped thin layers. Microring resonators with triangular cross section were optimized via simulation and etch development. The properties of the cavities were investigated by means of PL and CL scans. Emission spectra of the doped NV centers reveal prominent resonant lines on the NV sideband emission. While the quality of the devices remains to be improved and investigated in detail, the presented process enables for scalable fabrication of a large variety of photonic integrated circuits based on single-crystal diamond. In combination with highly NV-doped CVD layers, this will soon enable the implementation of heterointegrated photonic networks for highly sensitive diamond-based quantum sensing.

Spin-based quantum computing requires the local generation of single NVs in lateral waveguides.[23,24] A promising way to achieve the latter is via local implantation of nitrogen and will be the subject of future work.

Acknowledgements

This material was based upon work supported by the German Federal Ministry of Education and Research (BMBF) under grant no. 13NI6209 (Spinning). The authors also thank Lukas Lindner for the fruitful discussions.

Open Access funding enabled and organized by Projekt DEAL.

Conflict of Interest

The authors declare no conflict of interest.

Data Availability Statement

Research data are not shared.

Keywords

diamonds, dry etching, nitrogen vacancy centers, photonic integrated circuits, quantum sensing, ring resonators, waveguides

Received: June 9, 2023
Revised: September 24, 2023
Published online: April 15, 2024

[1] A. Gruber, A. Drabenstedt, C. Tietz, L. Fleury, J. Wrachtrup, C. von Borczyskowski, *Science* **1997**, *276*, 2012.
[2] M. V. Gurudev Dutt, L. Childress, L. Jiang, E. Togan, J. Maze, F. Jelezko, A. S. Zibrov, P. R. Hemmer, M. D. Lukin, *Science* **2007**, *316*, 1312.
[3] C. Kurtsiefer, S. Mayer, P. Zarda, H. Weinfurter, *Phys. Rev. Lett.* **2000**, *85*, 290.
[4] F. Jelezko, T. Gaebel, I. Popa, M. Domhan, A. Gruber, J. Wrachtrup, *Phys. Rev. Lett.* **2004**, *93*, 130501.
[5] M. W. Doherty, N. B. Manson, P. Delany, F. Jelezko, J. Wrachtrup, L. C. L. Hollenberg, *Phys. Rep.* **2013**, *528*, 1.
[6] P. Neumann, N. Mizuochi, F. Rempp, P. Hemmer, H. Watanabe, S. Yamasaki, V. Jacques, T. Gaebel, F. Jelezko, J. Wrachtrup, *Science* **2008**, *320*, 1326.
[7] P. E. Barclay, K. Fu, C. Santori, R. G. Beausoleil, *Opt. Express* **2009**, *17*, 9588.
[8] T. M. Babinec, B. J. Hausmann, M. Khan, Y. Zhang, J. R. Maze, P. R. Hemmer, M. Lončar, *Nat. Nanotechnol.* **2010**, *5*, 195.
[9] C. Santori, P. E. Barclay, K.-M. C. Fu, R. G. Beausoleil, S. Spillane, M. Fisch, *Nanotechnology* **2010**, *21*, 274008.
[10] S. Tomljenovic-Hanic, T. J. Karle, A. D. Greentree, B. C. Gibson, B. A. Fairchild, A. Stacey, S. Prawer, in *Optical Engineering of Diamond* (Eds: R.P. Mildren, J.R. Rabeau), Wiley-VCH, Weinheim, Germany **2013**.
[11] T. Schröder, S. L. Mouradian, J. Zheng, M. E. Trusheim, M. Walsh, E. H. Chen, L. Li, I. Bayn, D. Englund, *J. Opt. Soc. Am. B* **2016**, *33*, 65.
[12] A. Faraon, P. E. Barclay, C. Santori, K.-C. Fu, R. G. Beausoleil, *Nat. Photonics* **2011**, *5*, 301.
[13] A. Faraon, C. Santori, Z. Huang, K. C. Fu, V. M. Acosta, D. Fattal, R. G. Beausoleil, *New J. Phys.* **2013**, *15*, 025010.
[14] P. Latawiec, V. Venkataraman, M. J. Burek, B. J. M. Hausmann, I. Bulu, M. Lončar, *Optica* **2015**, *2*, 924.
[15] M. J. Burek, N. P. de Leon, B. J. Shields, B. J. M. Hausmann, Y. Chu, Q. Quan, A. S. Zibrov, H. Park, M. D. Lukin, M. Lončar, *Nano Lett.* **2012**, *12*, 6084.
[16] P. Latawiec, M. J. Burek, Y. Sohn, M. Lončar, *J. Vac. Sci. Technol. B* **2016**, *34*, 041801.
[17] C. Giese, P. Quellmalz, P. Knittel, *MRS Adv.* **2020**, *41*, 1.
[18] M. P. Hiscocks, K. Ganesan, B. C. Gibson, S. T. Huntington, F. Ladouceur, S. Prawer, *Opt. Express* **2008**, *16*, 19512.
[19] C. J. Widmann, M. Hetzl, S. Drieschner, C. E. Nebel, *Diamond Relat. Mater.* **2017**, *72*, 41.
[20] P. Schätzle, P. Reinke, D. Herrling, A. Götze, L. Lindner, J. Jeske, L. Kirste, P. Knittel, *Phys. Status Solidi A* **2023**, *220*, 2200351.
[21] B. Khanaliloo, M. Mitchell, A. C. Hryciw, P. E. Barclay, *Nano Lett.* **2015**, *15*, 5131.
[22] T. Luo, L. Lindner, J. Langer, V. Cimalla, X. Vidal, F. Hahl, C. Schreyvogel, S. Onoda, T. Ohshima, D. Wang, D. A. Simpson, B. C. Johnson, M. Capelli, R. Blinder, J. Jeske, *New J. Phys.* **2022**, *24*, 033030.
[23] M. Ruf, N. H. Wan, H. Choi, D. Englund, R. Hanson, *J. Appl. Phys.* **2021**, *130*, 70901.
[24] K. Nemoto, M. Trupke, S. J. Devitt, A. M. Stephens, B. Scharfenberger, K. Buczak, T. Nöbauer, M. S. Everitt, J. Schmiedmayer, W. J. Munro, *Phys. Rev. X* **2014**, *4*, 031022.

© 2023 The Authors. physica status solidi (a) applications and materials science published by Wiley-VCH GmbH

18626319, 2024, 8, Downloaded from https://onlinelibrary.wiley.com/doi/10.1002/pssa.202300433, Wiley Online Library on [24/04/2024]. See the Terms and Conditions (https://onlinelibrary.wiley.com/terms-and-conditions) on Wiley Online Library for rules of use; OA articles are governed by the applicable Creative Commons License